nature nanotechnology

Article

https://doi.org/10.1038/s41565-025-01983-4

A nanoengineered lithium-hosting carbon/zinc oxide composite electrode material for efficient non-aqueous lithium metal batteries

Received: 9 July 2024

Accepted: 25 June 2025

Published online: 29 July 2025

Check for updates

Lequan Deng[1], Yaoyao Liu[1], Haoying Qi[1], Yushuang Yang[1], Zhaofen Wang[1], Lu-Tan Dong[1], Jun Zhan[2], Ke-Peng Song[3], Dongqing Qi[3], Yayang Xu[1], Yuanhua Sang[1], Jinlong Yang[4], Jian-Jun Wang[1], Zhaoke Zheng[1], Shuhua Wang[1], Chao Gao[5] ✉, Hong Liu[1,2] ✉ & Hao Chen[1,6] ✉

Achieving Coulombic efficiency values greater than 99.9% for Li metal cells is considered one of the most important requirements for the technology development of long cycle life in energy-dense Li metal batteries. However, owing to the volume changes in Li metal electrodes and Li reservoir loss during battery operation, this requirement has not yet been realized in Li metal cells. Here, to overcome these issues, we propose a zero-volume-change, complete-sealing design for a nanoengineered composite material consisting of multilayer reduced graphene oxide and zinc oxide. This composite electrode material can accommodate Li metal without showing negligible volume changes while promoting the formation of an inorganic-rich solid-electrolyte interphase. When the nanoengineered Li/reduced graphene oxide/zinc oxide electrode is tested in combination with a Li metal electrode in a coin cell configuration using non-aqueous electrolyte solutions, Li plating/stripping Coulombic efficiency values ranging from 99.9900% to 99.9999%, for almost 2,000 cycles at a current density of 1 mA cm^{-2}, can be calculated. Testing of the nanoengineered Li/reduced graphene oxide/zinc oxide electrode in combination with high-potential electrodes (for example, $LiNi_{0.8}Co_{0.1}Mn_{0.1}O_2$ or $LiFePO_4$) in non-aqueous coin cell configuration also demonstrates improved performance compared with the high-potential coin cells utilizing pristine Li metal electrodes.

Li metal is the negative electrode active material of choice to increase the specific energy of non-aqueous Li-based batteries to 500 Wh kg^{-1}, owing to its highest theoretical specific capacity (3,860 mAh g^{-1}) and lowest electrode potential (−3.04 V versus standard hydrogen electrode)[1–3]. However, current Li metal negative electrode technology is limited by the low Li plating/stripping reversibility (experimentally evaluated via Coulombic efficiency (CE) calculations), which causes fast capacity decay, rapid electrode's active material loss and short cycle cell life[4]. A Li plating/stripping CE of >99.9% over 1,000 cycles in Li metal cells is a basic performance requirement to attain adequate cycle life, as reported and discussed in the literature[3,5,6]. However, this goal has not been fully achieved.

The reasons for the failure mechanisms of cells with a Li metal negative electrode are two: (i) the constant volume change of the Li metal electrode during repeated Li plating/stripping and (ii) the high chemical reactivity of metallic Li in contact with the electrolyte[4]. As shown in Fig. 1a,b, the surface of a non-passivated Li metal electrode is unstable against corrosion when in contact with a non-aqueous electrolyte

A full list of affiliations appears at the end of the paper. ✉e-mail: chaogao@zju.edu.cn; hongliu@sdu.edu.cn; haochen@sdu.edu.cn

https://doi.org/10.1038/s41565-025-01983-4

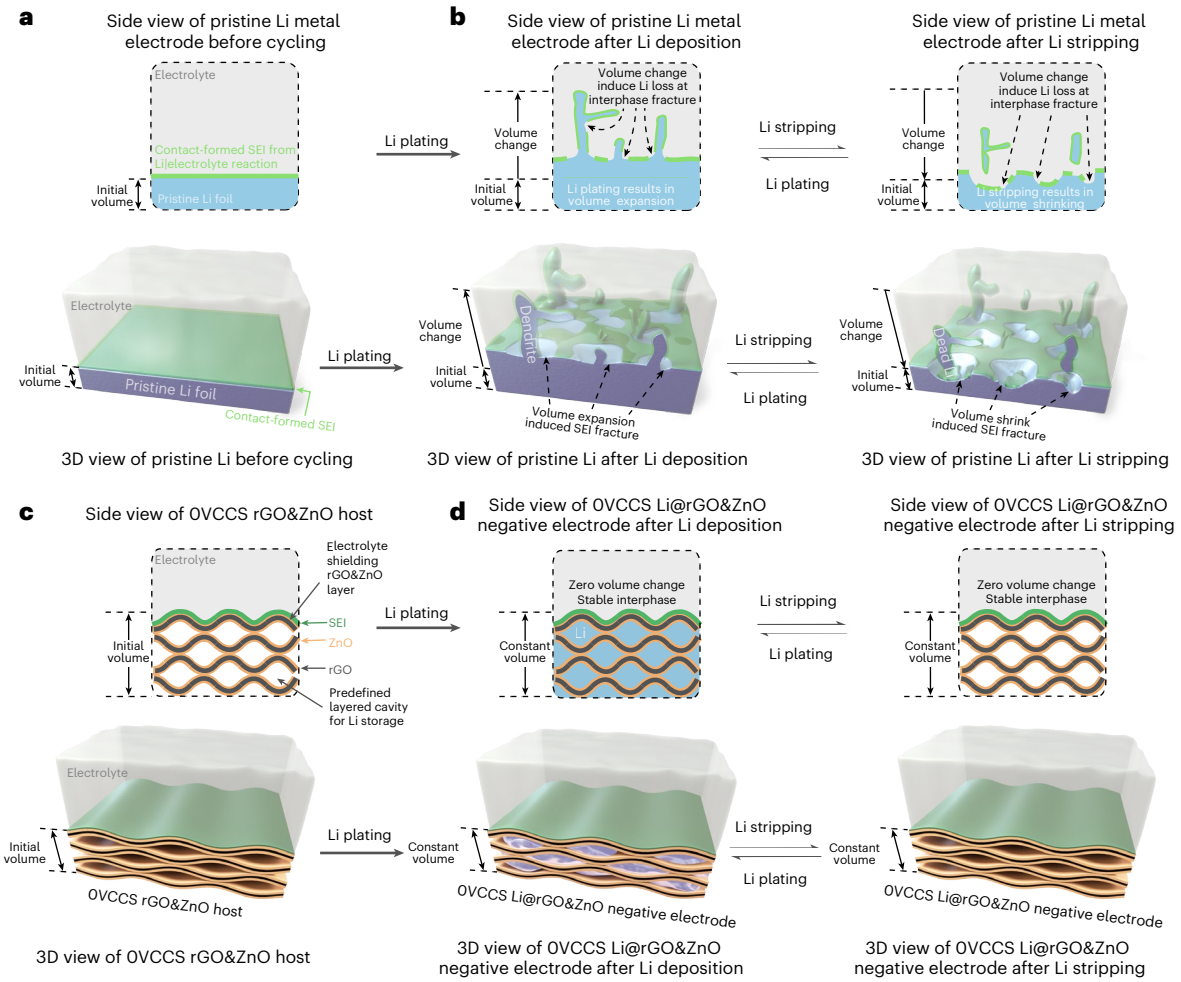

Fig. 1 | Nanoengineered carbon/ZnO composite design for Li metal hosting during electrochemical cycling. a, Schematic representation of contact-formed SEI on the Li metal electrode. **b**, Schematic representation of lithium electrodeposition on a pristine Li metal electrode, showing relative volume change and SEI mechanical damages that lead to Li|electrolyte side reaction and active material depletion during repeated Li plating/stripping processes. **c**, Schematic representation of the nanoengineered structure of the carbon/ZnO composite as Li-hosting electrode material. **d**, Schematic representation of the Li-hosting mechanism of the carbon/ZnO nanoengineered composite, showing shielding from electrolyte permeation, confined Li plating/stripping in the layered cavities, absence of volume change during Li plating/stripping and stable SEI.

solution. However, its surface is protected with the formation of the solid-electrolyte interphase (SEI), which is generated from the interaction between the Li metal electrode and the electrolyte solution[7,8]. The volume expansion and shrinking during repeated Li metal plating/stripping processes cause mechanical damage to the SEI, which exposes the inner non-passivated metallic Li to the electrolyte. This results in the depletion of the Li reservoir in the electrolyte and negative electrode, leading to rapid capacity decay in the cell (Fig. 1b). Uneven Li plating/stripping also preferentially occurs at the mechanically damaged SEI site[4,9–11]. Extensive research efforts have been devoted to improving the cycling reversibility of lithium metal cells, focusing on (i) the development of high-surface-area lithiophilic hosts at the negative electrode, aiming to decrease the detrimental effects of local current density and volume change[12,13], (ii) the engineering of robust artificial SEI to suppress SEI mechanical damages[14,15], (iii) the formulation of fluorinated non-aqueous electrolyte solutions to generate stable SEI and mitigate the depletion of the Li reservoir[16], (iv) the use of solid-state electrolytes to hinder Li dendrite growth during cell cycling[17,18], and (v) other emerging strategies[19,20]. Although the recent development of tailored electrolyte solutions, such as fluorinated electrolyte[21] and localized highly concentrated electrolyte (LHCE)[22], has demonstrated the ability to partially circumvent the issue of rapid depletion of the Li reservoir, the problem of the Li metal electrode volume change is not yet fully solved. Indeed, Li metal cells with prolonged average CE >99.9% have not yet been reported, and this aspect acts as a stumbling block for the development of long-life high-energy lithium metal batteries[7,23].

To circumvent the low CE issue in Li metal battery technology, here we propose a 'zero-volume-change complete-sealing' (0VCCS) Li-host nanoengineered composite electrode material, which enables an average CE >99.99% for almost 2,000 coin cell cycles when tested in combination with a Li metal counter electrode and an LHCE solution. The structural two-dimensional, continuous, layered, cavity-structured zinc oxide (ZnO)-coated reduced graphene oxide (rGO) architecture of the composite (Fig. 1c) facilitates confined Li plating/stripping while preventing Li reservoir loss (Fig. 1d). The nanoengineered architecture of the electrode material (labelled as 0VCCS Li@rGO&ZnO) enables a zero-volume-change feature during Li plating and stripping as demonstrated via operando electrochemical pressure sensing characterizations, and in situ and ex situ microscopy measurements. This volumetric feature promotes the formation of a mechanically stable SEI and effective Li metal protection, which enables an average CE >99.99% for Li||0VCCS Li@rGO&ZnO lab-scale coin cells tested using non-aqueous LHCE or conventional carbonate-based electrolyte solutions. When the 0VCCS Li@rGO&ZnO negative electrodes are tested in combination

https://doi.org/10.1038/s41565-025-01983-4

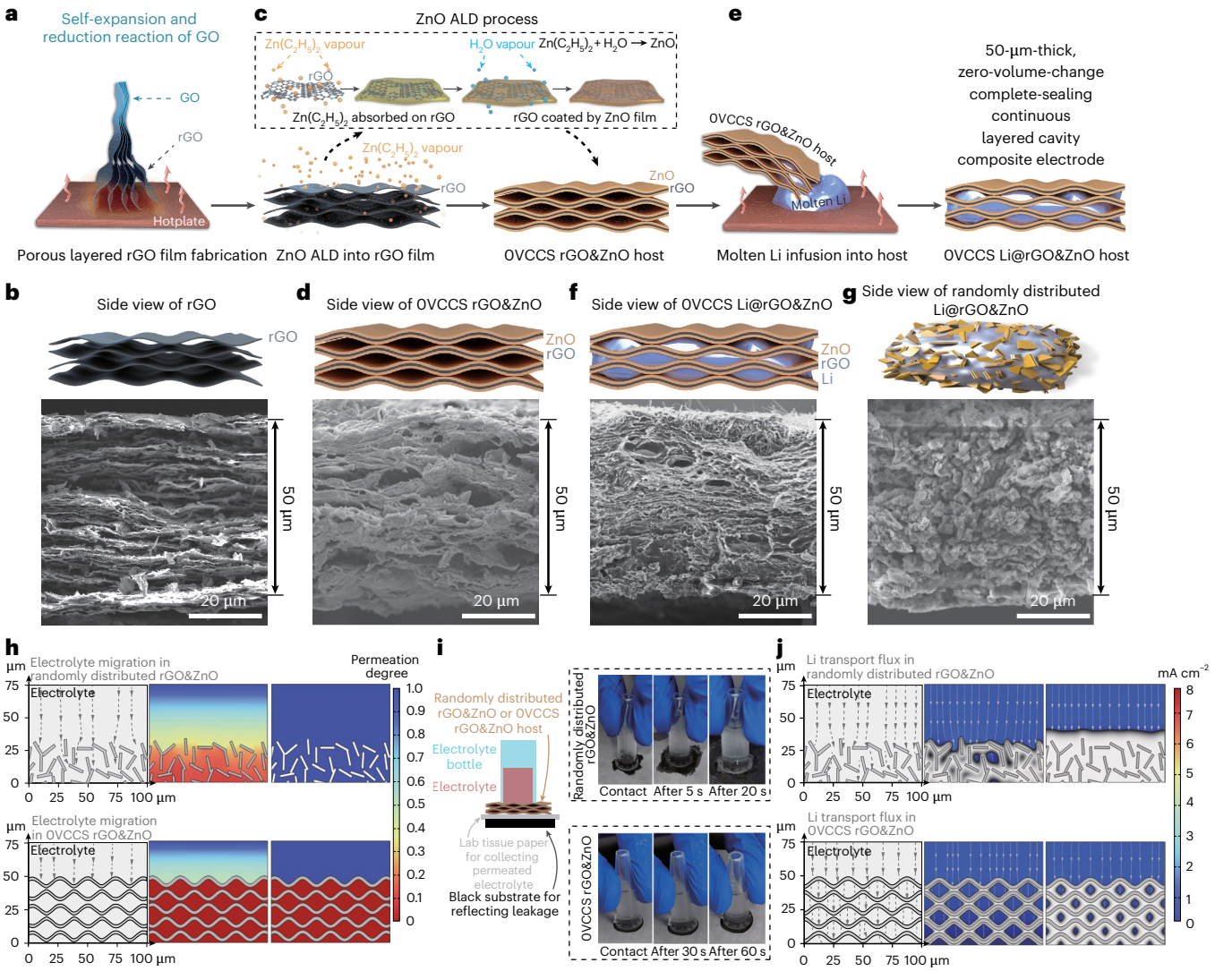

Fig. 2 | Fabrication and physicochemical characterizations of various rGO&ZnO composite structures. a, Schematic of the thermal reduction process applied to fabricate the porous layered rGO film. **b**, Cross-sectional SEM image of the thermally reduced porous layered rGO film showing a thickness of 50 μm. **c**, Schematic of the ZnO ALD process on the porous layered rGO film for fabricating the porous layered cavity-structured rGO&ZnO composite. **d**, Cross-sectional SEM image of the porous layered cavity-structured, 0VCCS rGO&ZnO composite after ALD of ZnO, showing a homogeneous thickness of 50 μm. **e**, Schematic representation of the molten Li infusion process into the porous layered 0VCCS rGO&ZnO host to fabricate the 0VCCS Li@rGO&ZnO electrode. **f**, Cross-sectional SEM image of the 0VCCS Li@rGO&ZnO electrode showing a thickness of 50 μm. **g**, Cross-sectional SEM image of the randomly distributed Li@rGO&ZnO electrode showing a thickness of 50 μm, with random distribution of the rGO&ZnO composite layers instead of the layered cavity structure. **h**, COMSOL simulation results on the electrolyte permeation behaviour in the randomly distributed rGO&ZnO and 0VCCS rGO&ZnO hosts. **i**, Schematic and photographic pictures of the electrolyte permeation tests of the randomly distributed rGO&ZnO and 0VCCS rGO&ZnO host. A clear bottle containing 1 ml of electrolyte is placed over the 0VCCS rGO&ZnO or randomly distributed rGO&ZnO host, and a piece of thin lab tissue paper (main component is plant cellulose fibre) for collecting the leaked electrolyte and a black solid wood table substrate for reflecting electrolyte collection are placed underneath the host, as the electrolyte-swelled lab tissue paper can realize minor semi-transparence for showing the colour of black substrate underneath. That is, if a black substrate is shown, it indicates that the electrolyte is leaking; if it is not shown, it indicates that there is no leakage. **j**, COMSOL simulations of Li plating behaviour in the randomly distributed rGO&ZnO and 0VCCS rGO&ZnO host.

with $LiNi_{0.5}Co_{0.2}Mn_{0.3}O_2$- and $LiFePO_4$-based positive electrodes in a coin cell configuration using non-aqueous electrolyte solutions, the battery cycling life is improved compared with similar cells equipped with pure Li metal or non-nanoengineered composite negative electrodes.

Preparation, physicochemical and electrochemical characterizations of the nanoengineered Li-hosting carbon/ZnO composite electrodes

The 0VCCS Li@rGO&ZnO negative electrode was fabricated by molten Li infusion into the layered cavity-structured lithiophilic host structure (Fig. 2a). Applying a reduction reaction on a graphene oxide (GO) film[24], a 50-μm-thick porous layered rGO film template (with an area of about 50 cm^2) was fabricated (Fig. 2b and Supplementary Figs. 1 and 2). After that, diethylzinc and water vapours were alternately pulsed into the porous rGO film template, absorbed onto the rGO layer and purged out using an industrial-level atomic layer deposition (ALD) fabrication procedure (Fig. 2c), converting into a uniform ZnO film that covers the rGO matrix and fills the structural defects in rGO, as shown by the transmission electron microscopy (TEM) micrographs in Supplementary Figs. 3–5. After 800 cycles of ALD, 365-nm-thick ZnO layers were uniformly coated on the 30-nm-thick multilayer rGO structure inside

the porous host, as illustrated by both scanning electron microscopy (SEM; Supplementary Figs. 6 and 7) and atomic force microscopy (AFM; Supplementary Figs. 8 and 9) measurements, while the whole rGO&ZnO composite maintains the initial thickness of 50 µm (Fig. 2d). A top-view (SEM) micrograph (Supplementary Fig. 10) of the rGO&ZnO composite shows the morphology of the ZnO coating on the rGO, characterized by a compact structure. The comparison of Young's moduli measured with the AFM measurements shows an improvement in the mechanical properties of the electrodes comprising the rGO&ZnO composite compared with those entirely based on rGO and Li metal (Supplementary Fig. 11). After the edge-contacting molten Li infusion process[12] (Fig. 2e), metallic Li was confined inside the microscale cavities in the multilayered rGO&ZnO structure forming a 50-µm-thick Li@rGO&ZnO composite electrode active material (0VCCS Li@rGO&ZnO) as shown in Fig. 2f and Supplementary Fig. 12. This electrode design is conceived to make use of commercially available raw materials (such as GO dispersions) and established industrial technologies (such as ALD[25,26]) for possible future large-scale fabrications. To prove the structural and mechanical effectiveness of the 0VCCS Li@rGO&ZnO, we also fabricate a Li@rGO&ZnO composite electrode via molten Li infusion into a randomly distributed rGO&ZnO composite (prepared through an ultrasonication method), which does not show layered cavity structures (Fig. 2g). X-ray diffraction (XRD) and X-ray photoelectron spectroscopy (XPS) measurements evidence the structural and chemical composition changes upon the composite fabrication procedures from the multilayer rGO film to the rGO&ZnO composite (0VCCS rGO&ZnO host), and finally to the 0VCCS Li@rGO&ZnO composite electrode material, which also comprise LiZn and Li_2O (Supplementary Figs. 13 and 14). COMSOL simulations (Fig. 2h) suggest that the electrolyte solution can penetrate into the randomly distributed rGO&ZnO host, thus failing to fully protect the lithium metal. By contrast, the multilayered continuous structure of the 0VCCS rGO&ZnO host can effectively prevent the permeation of the electrolyte into the host to react with metallic Li. The simulation results are experimentally verified via the electrolyte infiltration test (Fig. 2i), where the randomly distributed rGO&ZnO host shows rapid electrolyte penetration across the thickness of the host. By contrast, no electrolyte permeation was detected after sealing the electrolyte-containing vial with the nanoengineered 0VCCS rGO&ZnO host, thus demonstrating its Li protection function against electrolyte permeation. In addition, COMSOL simulations (Fig. 2j) on the Li deposition behaviour in the randomly distributed rGO&ZnO host show that these metallic Li depositions are highly exposed to the electrolyte, which leads to substantial volume change in the electrode. In comparison, metallic Li can be uniformly deposited inside the layered cavities of the 0VCCS rGO&ZnO host, protecting the deposited Li from contact with the electrolyte solution with negligible changes in the electrode volume after Li metal deposition (Fig. 2j).

The effects of the 0VCCS host design on the cells' CE and cycling performance were evaluated in Li||host coin cell configurations, after complete electrochemical stripping of metallic Li from the Li@host composite (using LHCE composed of lithium bis(fluorosulfonyl)imide (LiFSI), 1,2-dimethoxyethane (DME) and 1,1,2,2-tetrafluoroethyl-2,2,3,3-tetrafluoropropyl ether (TTE) with a molar ratio of 1:1.2:3 (ref. 22), under testing temperature of 25 °C ± 0.2 °C), as confirmed by XRD measurements (Supplementary Fig. 15), which corresponds to an areal capacity of stored metallic Li of around 7 mAh cm^{-2} in both 50-µm-thick 0VCCS Li@rGO&ZnO and 50-µm-thick randomly distributed Li@rGO&ZnO composite electrodes (Supplementary Fig. 16). Using the LHCE solution[22] mentioned above, the Li||0VCCS rGO&ZnO cell shows an average CE of 99.99005% during the initial 1,033 cycles (Fig. 3a and Supplementary Fig. 17). In the subsequent 916 cycles, the Li||0VCCS rGO&ZnO cell shows an average CE of 99.99995%. Moreover, between the 250th and 1,800th cycles, the Li||0VCCS rGO&ZnO cell exhibits a potential hysteresis in the 50–83 mV range (Fig. 3b). In comparison, the Li metal cell with the randomly distributed rGO&ZnO host shows a lower average CE of 94.92028% and larger potential hysteresis in the 58–129 mV range for 417 cycles, short-circuiting after the 418th cycle (Fig. 3c and Supplementary Fig. 18a,b). Also, the Li metal cell with the pure rGO host enables an average CE of 97.18056% for 300 cycles (Supplementary Fig. 19), while the Li metal cell using pristine copper as the counter electrode exhibited an average CE of 99.23930% for 1,064 cycles before short-circuiting (Fig. 3c and Supplementary Fig. 18c,d). Via titration gas chromatography measurements, we demonstrate that the main Li-ion storage mechanism in Li||0VCCS rGO&ZnO cells is Li plating and stripping at both two kinds of different cell's cut-off charging potentials: 0.09 V and 1 V (Fig. 3b and Supplementary Figs. 20–22; detailed explanations in Supplementary Notes 1–3). Using the Aurbach method[27] to evaluate the CE of various Li metal cell configurations, we calculate an average CE value as high as 99.99999% for the Li||0VCCS rGO&ZnO cell, which exceeds those of Li metal cells with randomly distributed rGO&ZnO and copper electrodes (Supplementary Figs. 23 and 24). At a current density of 3 mA cm^{-2} and a capacity of 3 mAh cm^{-2} (Supplementary Fig. 25), the Li||0VCCS rGO&ZnO cell with LHCE shows a high average CE of 99.99053% over 400 cycles, along with stable potential hysteresis (in the range of 171–193 mV). In addition, when a conventional carbonate-based non-aqueous electrolyte solution (1 M $LiPF_6$ in ethylene carbonate (EC)/diethyl carbonate (DEC) with fluoroethylene carbonate (FEC) and vinylene carbonate (VC) additives) is used for the testing of the Li||0VCCS rGO&ZnO cell, an average CE of up to 99.99992% can be calculated (Fig. 3d and Supplementary Fig. 26). This CE value is higher than that obtained in Li||randomly distributed rGO&ZnO (average CE = 83.15887%) and Li||Cu (average CE = 95.17104%) cells with the carbonate electrolyte solution (Fig. 3d and Supplementary Fig. 27). Compared with selected published research works available in the literature, where non-aqueous lab-scale cells containing Li metal and rGO-based host electrodes show average CEs within the 99.00–99.75% range (Supplementary Fig. 28 and Supplementary Table 1), the Li||0VCCS rGO&ZnO CE results provided in the present work (Fig. 3a) indicate a substantial improvement at the lab-scale low-operating-potential cell level.

After 2 activation cycles at 8.25 mA g^{-1} (Supplementary Fig. 29), the galvanostatic cycling of a 50-µm-thick (7.036 mAh cm^{-2}) 0VCCS Li@rGO&ZnO||$LiNi_{0.5}Co_{0.2}Mn_{0.3}O_2$ (NCM523, 3.06 mAh cm^{-2}) coin cell (using LHCE electrolyte) with a negative/positive electrode capacity ratio ($R_{N/P}$) of 2.3 (Fig. 3e and Supplementary Fig. 30) shows an 88.779% specific discharge capacity retention after 727 cycles at 82.5 mA g^{-1} by dividing the discharge capacity of the initial cycle under the condition of a specific current of 82.5 mA g^{-1} (156.483 mAh g^{-1}, 1st cycle in Fig. 3e) by the discharge capacity of the 727th cycle in Fig. 3e (138.924 mAh g^{-1}) under a specific current of 82.5 mA g^{-1}, along with stable potential profiles (Supplementary Fig. 31), an averaged CE of 99.74641% and with some erratic behaviour regarding cell discharge capacities and CEs (Fig. 3e and Supplementary Fig. 30). By contrast, the randomly distributed Li@rGO&ZnO||NCM523 ($R_{N/P}$ = 2.3), 50-µm-thick Li||NCM523 (10 mAh cm^{-2}, $R_{N/P}$ = 3.3) and Li@rGO||NCM523 ($R_{N/P}$ = 2.57) show 80% specific discharge capacity retention after 139 cycles (averaged CE of 99.78107%), 138 cycles (averaged CE of 99.52640%; Fig. 3f) and 162 cycles (averaged CE of 99.65193%; Supplementary Figs. 32 and 33), respectively, at the same specific current cycling conditions. Moreover, the galvanostatic cycling of a 50-µm-thick 0VCCS Li@rGO&ZnO||$LiFePO_4$ (LFP, 3 mAh cm^{-2}, $R_{N/P}$ = 2.3) coin cell exhibited 87.923% specific discharge capacity retention after 990 cycles by dividing the discharge capacity of the initial cycle under the condition of a specific current of 75 mA g^{-1} (140.684 mAh g^{-1}, 1st cycle in Fig. 3f) by the discharge capacity of the 990th cycle in Fig. 3f (123.694 mAh g^{-1}) under a specific current of 75 mA g^{-1} (Fig. 3f and Supplementary Fig. 34) with stable potential profiles (Supplementary Fig. 35), averaged CE of 99.96339% and with some erratic behaviour regarding cell discharge capacities and CEs (Fig. 3f and Supplementary Fig. 34), after 2 activation cycles at 7.5 mA g^{-1} (Supplementary

https://doi.org/10.1038/s41565-025-01983-4

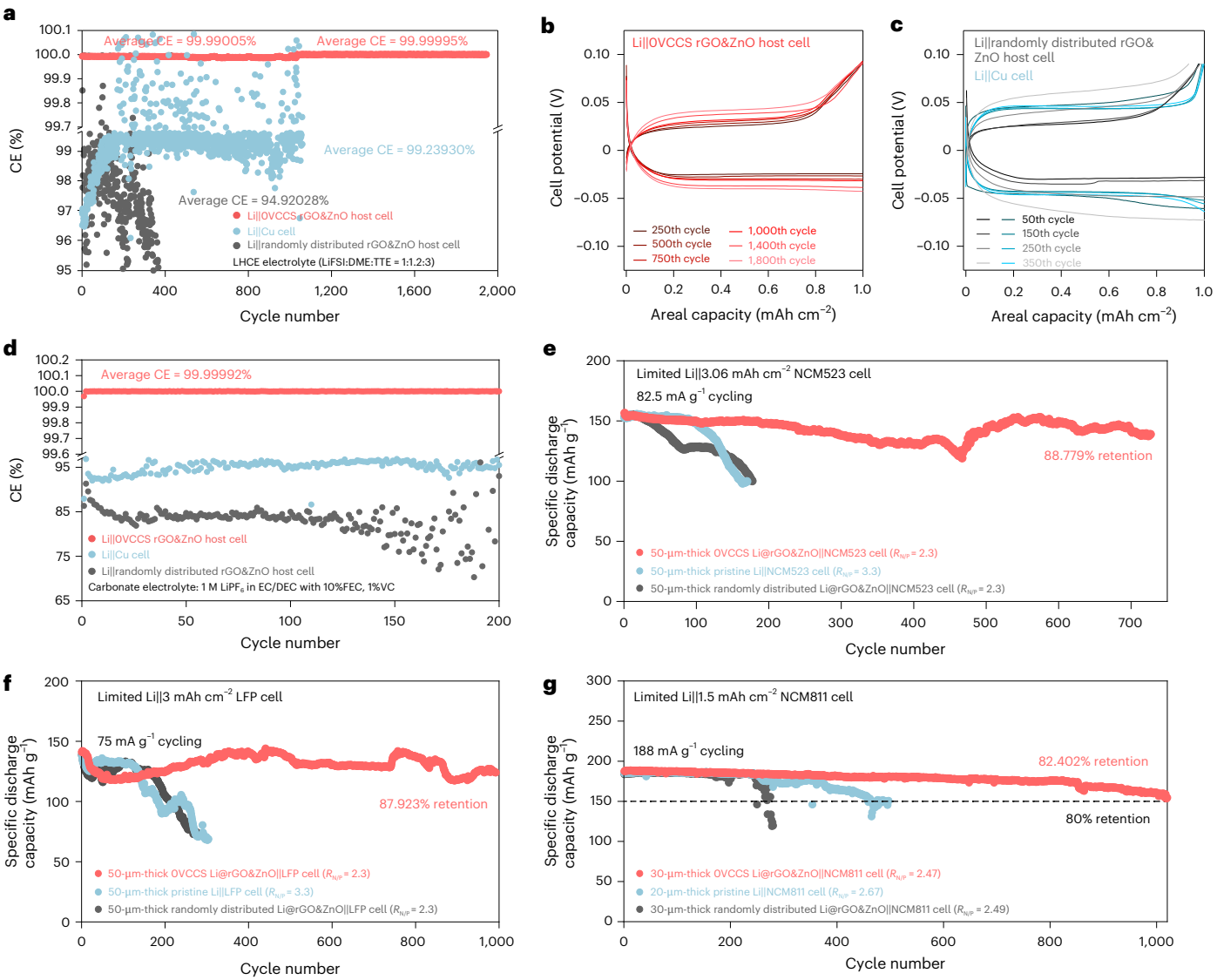

Fig. 3 | Electrochemical energy storage performances of non-aqueous Li metal cells in various configurations at 25 °C ± 0.2 °C. a, CE of Li||0VCCS rGO&ZnO host, Li||Cu and Li||randomly distributed rGO&ZnO coin cells cycled at 1 mA cm^{-2}, 1 mAh cm^{-2} using LHCE electrolyte (see Supplementary Fig. 17 for the magnified view of the Li||0VCCS rGO&ZnO host coin cell CE values). **b**, Potential profiles of a Li||0VCCS rGO&ZnO coin cell at various cycles (1 mA cm^{-2}, 1 mAh cm^{-2}). **c**, Potential profiles of Li||Cu and Li||randomly distributed rGO&ZnO coin cells at various cycles (1 mA cm^{-2}, 1 mAh cm^{-2}). **d**, CE of Li||0VCCS rGO&ZnO, Li||Cu and Li||randomly distributed rGO&ZnO coin cells cycled at 1 mA cm^{-2}, 1 mAh cm^{-2} using conventional carbonate electrolyte (see Supplementary Fig. 26 for the magnified view of the Li||0VCCS rGO&ZnO host coin cell CE values). **e**, Cycling stability of 50-μm-thick Li||3.06 mAh cm^{-2} $LiNi_{0.5}Co_{0.2}Mn_{0.3}O_2$ coin cells using various negative electrodes with strict negative/positive electrode capacity ratio ($R_{N/P}$) (that is, 0VCCS Li@rGO&ZnO, randomly distributed Li@rGO&ZnO and pristine Li metal) at a constant specific current of 82.5 mA g^{-1} and a potential cut-off range of 3.0–4.35 V. **f**, Cycling stability of 50-μm-thick Li||3 mAh cm^{-2} $LiFePO_4$ coin cells using various negative electrodes with strict negative/positive electrode capacity ratio ($R_{N/P}$) (that is, 0VCCS Li@rGO&ZnO, random Li@rGO&ZnO and pristine Li metal) at a constant specific current of 75 mA g^{-1} and a potential cut-off range of 2.5–4.0 V. **g**, Cycling stability of limited Li||1.5 mAh cm^{-2} $LiNi_{0.8}Co_{0.1}Mn_{0.1}O_2$ coin cells using various negative electrodes with strict negative/positive electrode capacity ratio ($R_{N/P}$) (that is, 0VCCS Li@rGO&ZnO, randomly distributed Li@rGO&ZnO and pristine Li metal) at a constant specific current of 188 mA g^{-1} and a potential cut-off range of 3.0–4.3 V. Capacity retention calculated as (initial discharge capacity)/(last cycle discharge capacity) in the figure, and the two activation cycles at low current were not considered but are shown in Supplementary Figs. 29, 36 and 43.

Fig. 36). By contrast, the randomly distributed Li@rGO&ZnO||LFP ($R_{N/P}$ = 2.3) and 50-μm-thick Li||LFP (10 mAh cm^{-2}, $R_{N/P}$ = 3.3) cells show 80% specific discharge capacity retention after 192 (averaged CE of 99.62166%) and 151 cycles (averaged CE of 99.89358%; Fig. 3f), respectively, at the same specific current cycling conditions. We attribute the erratic behaviour of the discharge capacities (Fig. 3e,f) and CEs (Supplementary Figs. 30 and 34) of coin cells containing NCM523 and LFP electrodes to a major extent to electrolyte depletion in the cell during cycling. To a lesser extent, we also consider unexpected power outages and computer malfunctions experienced in our laboratories during electrochemical measurements as contributing factors (Supplementary Note 4). To support these assumptions, in Supplementary Figs. 37 and 38, we report the specific discharge capacity and CE values of multiple 0VCCS Li@rGO&ZnO||NCM523 and 0VCCS Li@rGO&ZnO||$LiFePO_4$ coin cells tested in simultaneous measurements. The erratic behaviour is consistently present, which qualitatively supports the assumption that electrolyte depletion in the porous structures of the separators and positive electrodes acts as a major stumbling block to achieving regular cell discharge performances. This consideration is further supported by the ex situ visual inspection of

cell components, after prolonged cycling, which are essentially unwetted (see photographic pictures in Supplementary Fig. 39 and detailed discussion in Supplementary Note 5). To demonstrate the detrimental effect of an unoptimized positive electrode formulation on the cell cycling performance, we assembled and tested 3.71 mAh cm^{-2} 0VCCS Li@rGO&ZnO||1.5 mAh cm^{-2} $LiNi_{0.8}Co_{0.1}Mn_{0.1}O_2$ (NCM811) coin cells ($R_{N/P}$ = 2.47) as shown in Fig. 3g. These cells attain a specific discharge capacity retention of 82.402% after 1,020 cycles at 188 mA g^{-1} with an averaged CE of 99.41251% and a non-erratic cell discharge cycling behaviour which can be also noticed for the Li@rGO&ZnO||NCM811 ($R_{N/P}$ = 2.67, 80% retention after 465 cycles at 188 mA g^{-1}, averaged CE of 98.40971%) and random Li@rGO&ZnO|| NCM811 ($R_{N/P}$ = 2.49, 80% retention after 276 cycles at 188 mA g^{-1}, averaged CE of 97.43042%) cells (Supplementary Figs. 40–43).

The zero-volume-change and confined Li plating/stripping behaviour in the 0VCCS host is investigated via ex situ cross-sectional SEM and in situ optical microscopy measurements. When Li is fully stripped from the 50-µm-thick 0VCCS Li@rGO&ZnO electrode (Fig. 4a and Supplementary Fig. 44), it exhibits a constant thickness of 50 µm with layered cavity structure surrounded by the nanoengineered rGO&ZnO sheets (Fig. 4b). After Li plating, the metallic Li is deposited back into the cavities of the 50-µm-thick 0VCCS structure (Fig. 4c) and no metallic Li deposition is observed on the top surface of the host (Supplementary Fig. 45). Even after 400 repeated cycles of lithium plating/stripping (current density of 1 mA cm^{-2} and areal capacity of 1 mAh cm^{-2} using LHCE electrolyte, charging potential cut-off at 0.09 V), the 0VCCS Li@rGO&ZnO electrode maintains a constant thickness of 50 µm and uniform dendrite-free Li distribution inside the host (Fig. 4d). A magnified SEM micrograph in Fig. 4e shows the 0VCCS Li@rGO&ZnO layered lithium-hosting composite structure with no detectable presence of metallic Li on the external surface of the 0VCCS composite electrode as also shown in Supplementary Figs. 46–48. In comparison, the 50-µm-thick randomly distributed Li@rGO&ZnO structure (Fig. 4f) demonstrates a thickness decrease to 18.9 µm and 25.1 µm (corresponding to a 62.2% and 49.8% volume change compared with the initial 50-µm-thick randomly distributed Li@rGO&ZnO electrode thickness), when lithium is fully stripped and plated, respectively (Fig. 4g,h). After 200 cycles (current density of 1 mA cm^{-2} and areal capacity of 1 mAh cm^{-2} using LHCE electrolyte, potential upper cut-off at 0.09 V), the thickness of the randomly distributed Li@rGO&ZnO structure is 30.3 µm (corresponding to a 39.4% volume change compared with the initial Li@rGO&ZnO thickness; Fig. 4i) with a detectable amount of Li metal deposited on the external surface of the randomly distributed Li@rGO&ZnO structure. A magnified SEM micrograph in Fig. 4j shows that the randomly distributed rGO&ZnO composite in the electrode is mainly responsible for the loss of zero-volume-change and confined lithium plating/stripping.

The mechanical integrity of the SEI formed on the 0VCCS host structure is investigated via ex situ XPS electrode measurements after the initial Li stripping (Fig. 4k). On the outer SEI layer surface of the 0VCCS Li@rGO&ZnO electrode, carbon (C–C, 284.6 eV in C 1*s* spectra; C–O, 285.45 eV in C 1*s* spectra and 533.3 eV in O 1*s* spectra) and fluorine peaks (LiF, 685 eV in F 1*s* spectra and 56 eV in Li 1*s* spectra; CF_x, 688 eV in F 1*s* spectra) are detected, suggesting an organic electrolyte solution-derived SEI containing carbon and fluorine elements. However, after multiple sputtering (Fig. 4k), the organic electrolyte solution-derived carbon and fluorine peaks disappear. The inner SEI layer of the 0VCCS rGO&ZnO electrode shows a different composition with peaks mostly associated with inorganic compounds (LiZn-related peak at 52.2 eV in Li 1*s* spectra and 1,018.7 eV in Zn 2*p* spectra; Li_2O-related peak at 53.6 eV in Li 1*s* spectra and 528.3 eV in O 1*s* spectra; ZnO-related peak at 1,020.8 eV in Zn 2*p* spectra; negligible amount of rGO-related peak at 282.2 eV and 289.15 eV in C 1*s* spectra). These XPS depth profiles reveal a bilayer SEI structure with an electrolyte solution-derived organic outer layer and a 0VCCS Li@rGO&ZnO-derived inorganic inner layer (Fig. 4l). The absence of organic electrolyte solution-derived components in the inner inorganic-rich SEI layer suggests a beneficial effect on the overall SEI mechanical properties and validates the assumption that the electrolyte solution does not penetrate the inner regions of the 0VCCS Li@rGO&ZnO composite. In comparison, the randomly distributed Li@rGO&ZnO electrode shows a constant electrolyte solution-derived organic-rich distribution across the whole SEI thickness, with a noticeable presence of carbon- and fluorine-based components (LiF, 685 eV in F 1*s* spectra and 56 eV in Li 1*s* spectra; C=O and S=O, 531.9 eV in O 1*s* spectra; C–C, 284.6 eV in C 1*s* spectra), and a lower amount of rGO&ZnO-derived species (Fig. 4m,n). The results of the ex situ XPS measurements and analyses thus suggest that the 0VCCS electrode material design can overcome the issues associated with the mechanical integrity and stability of SEI during prolonged Li stripping/plating, also inhibiting the permeation of the electrolyte solution into the Li-hosting rGO&ZnO structure.

We also investigated the volume-change feature of various Li-hosting negative electrodes in combination with a $Li_4Ti_5O_{12}$ (LTO) positive electrode in multilayer pouch cell configuration via operando battery pressure sensing characterizations[20,28]. As shown in Fig. 5a, a Li||LTO pouch cell containing 3 layers of double-side-coated LTO-based positive electrodes (areal capacity of 3.1 mAh cm^{-2} in each side), 6 layers of 50-µm-thick Li-hosting negative electrodes and 6 layers of porous trilayer polypropylene/polyethylene/polypropylene separator (Celgard 2325) with 500 µl non-aqueous LHCE solution was clamped between two metal force-distribution plates in the split cell with an initial uniaxial stack pressure of about 440 kPa, and a real-time data-collecting pressure sensor was utilized to monitor the stack pressure changes of the Li||LTO pouch cell during battery operation[28]. Considering the 'zero-strain' feature of LTO as an electrode active material, the pressure change of the various Li||LTO pouch cells during charging and discharge is arbitrarily attributed only to the volume change happening at the Li-hosting negative electrodes[29]. As shown in Fig. 5b, the stack pressure applied on the pristine Li||LTO pouch cell decreases from 436 kPa to 50 kPa during the discharging process. This pressure decrease is associated with the volume shrinkage happening at the negative electrode because of the Li metal stripping process (Fig. 5c). After the subsequent Li plating and cell's charging process, the stack pressure of the pristine Li||LTO pouch cell increased to 517 kPa. This pressure value, which is higher than the initial applied stacking pressure, is caused by the volume expansion and formation of porous Li metal structures during the Li plating process. The volume change leads to mechanical instability of the SEI and favours the Li|electrolyte side reactions. These latter detrimentally affect the cell's CE and Li metal reservoir[4] (Fig. 5c). Incorporating a randomly distributed rGO&ZnO composite host into the Li metal negative electrode only partially mitigates the volume-change issue, as proved by the smaller pressure variation during battery operation (initial stack pressure of 441 kPa, 97 kPa under discharged state and 444 kPa under charged state). In comparison, the 0VCCS Li@rGO&ZnO||LTO pouch cell exhibits very constant pressure during the initial Li stripping and plating step (Fig. 5b, 438 kPa at initial discharge state, 438 kPa after full discharge and 438 kPa after full charge), demonstrating the successful realization of zero-volume-change feature for the nanoengineered 0VCCS Li@rGO&ZnO electrodes. In the subsequent pouch cell cycles (Fig. 5d), the 0VCCS Li@rGO&ZnO negative electrode does not undergo volume change as demonstrated by the stable stack cell pressure value at 438 kPa. By contrast, the pouch cells with the pristine Li metal and randomly distributed Li@rGO&ZnO negative electrodes show noticeable pressure fluctuation (434–505 kPa at charged state and 36–38 kPa at discharged state for the pristine Li||LTO pouch cell; 441–449 kPa at charged state and 96–100 kPa at discharged state for the randomly distributed Li@rGO&ZnO||LTO pouch cell). At a lower stacking pressure of about 90 kPa, the zero-volume-change feature of the 0VCCS Li@rGO&ZnO electrode is also retained during repeated Li||LTO pouch cell cycling. By contrast, the pouch cells with pristine Li

https://doi.org/10.1038/s41565-025-01983-4

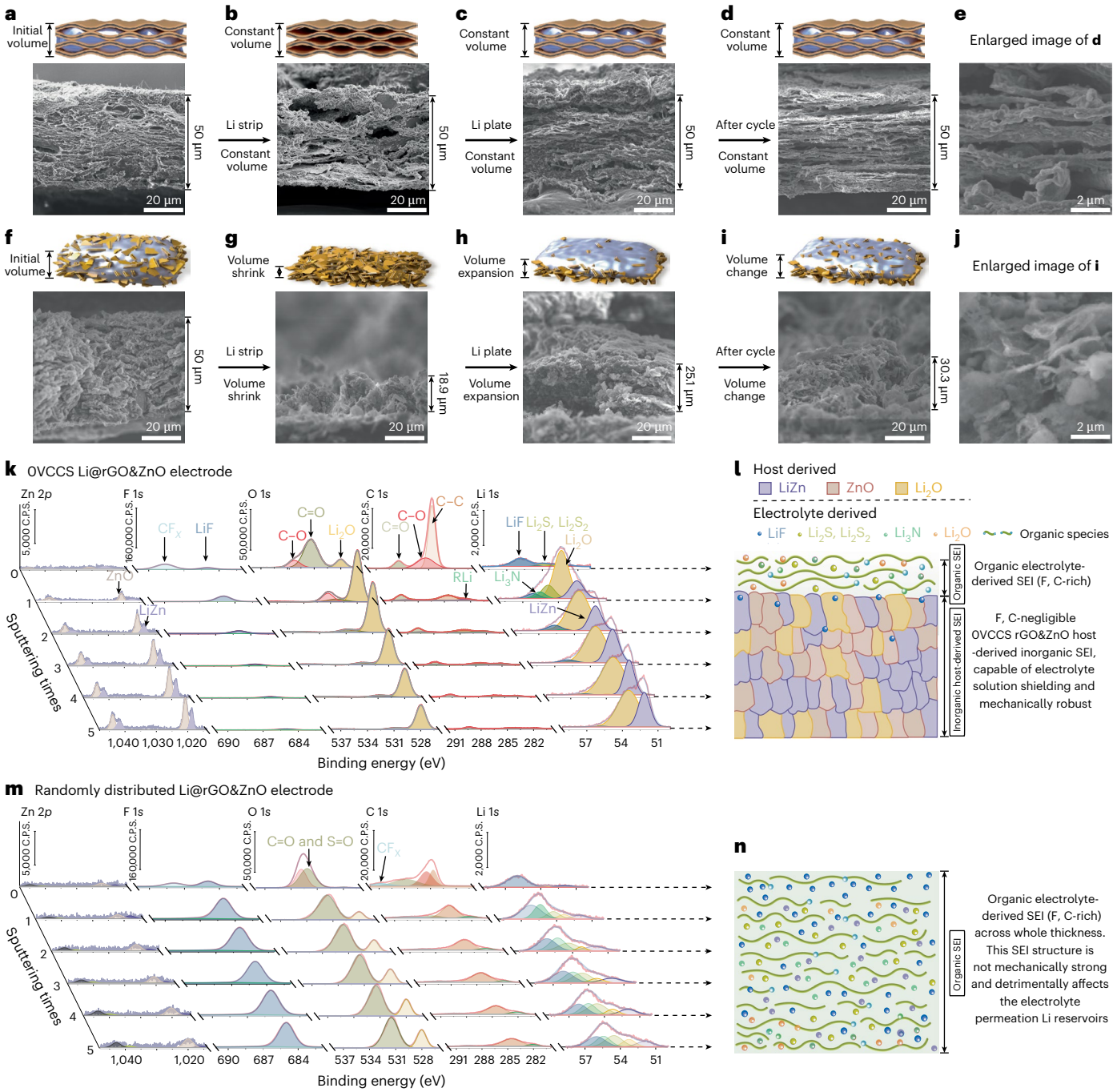

Fig. 4 | Morphological and chemical characterizations of 0VCCS and randomly distributed Li@rGO&ZnO electrodes during cycling. a, Cross-sectional SEM micrograph and three-dimensional (3D) schematic of pre-cycling 50-μm-thick 0VCCS Li@rGO&ZnO electrode and two-dimensional continuous layered composite structure. Panel **a** presents reduced-magnification SEM image relative to Fig. 2f, as both figures depict the same 0VCCS Li@rGO&ZnO electrode at the same stage (after complete electrode fabrication and before cycling in coin cell configuration). **b**, Cross-sectional SEM micrograph and 3D schematic of 0VCCS Li@rGO&ZnO electrode after initial Li stripping: constant 50-μm-thick with internal voids between structural two-dimensional continuous rGO&ZnO layers. **c**, Cross-sectional SEM micrograph and 3D schematic of 0VCCS Li@rGO&ZnO electrode after Li plating: constant 50-μm-thick with inner voids filling. **d**, Cross-sectional SEM micrograph and 3D schematic of a 0VCCS Li@rGO&ZnO electrode after 400 cycles: constant 50-μm-thick with stable layered Li composite structure. **e**, Magnified SEM micrograph of **d**. **f**, Cross-sectional SEM micrograph and 3D schematic of pre-cycling 50-μm-thick Li@rGO&ZnO electrode, with random distribution of metallic Li and rGO&ZnO layers. **g**, Cross-sectional SEM micrograph and 3D schematic of randomly distributed 18.9-μm-thick Li@rGO&ZnO electrode after Li stripping showing volume change and collapsed host structure. **h**, Cross-sectional SEM micrograph and 3D schematic of a randomly distributed 25.1-μm-thick Li@rGO&ZnO electrode after Li plating showing top-side Li deposition. **i**, Cross-sectional SEM micrograph and 3D schematic of randomly distributed 30.3-μm-thick Li@rGO&ZnO electrode after 200 cycles. **j**, Magnified SEM micrograph of **i** showing the random distribution of rGO&ZnO layers without structural two-dimensional continuity. **k**, Ex situ XPS depth profile of 0VCCS Li@rGO&ZnO electrode SEI composition after full Li stripping (counts per second (C.P.S.) is the unit of intensity). **l**, Reconstructed SEI chemical composition/distribution of the 0VCCS host from XPS depth profiles: light green square indicates electrolyte penetration. **m**, Ex situ XPS depth profile of SEI composition in randomly distributed Li@rGO&ZnO after full Li stripping (C.P.S. is the unit of intensity). **n**, Reconstructed SEI chemical composition/distribution in randomly distributed host from XPS depth profiles: light green square indicates electrolyte swelling into SEI[32] (for these ex situ measurements, all the cell configurations were the same as the Li||host coin cell (Methods) with LHCE solution under testing temperature of 25 °C ± 0.2 °C; charging cut-off potential, 0.09 V; current density, 1 mA cm^{-2}).

https://doi.org/10.1038/s41565-025-01983-4

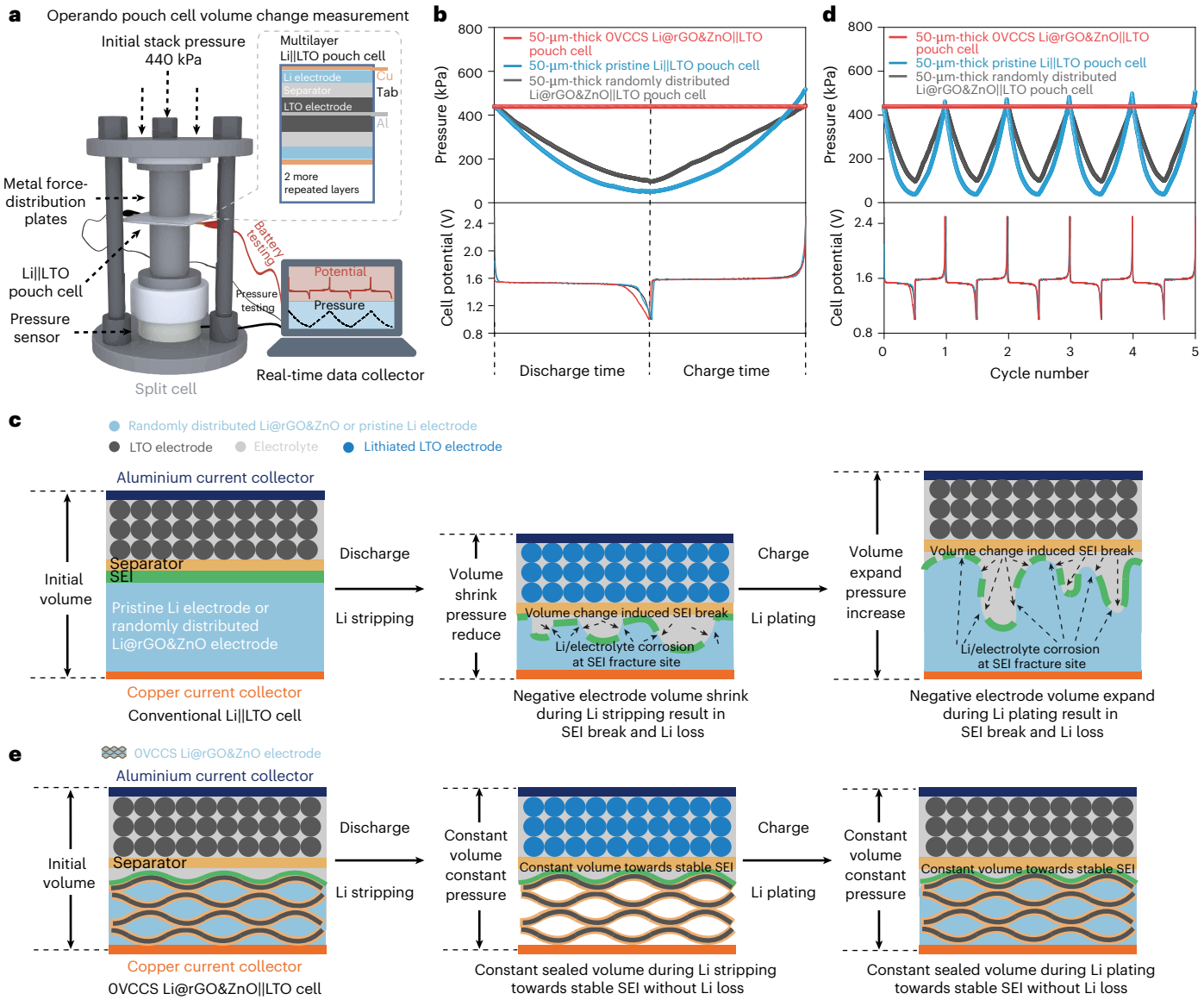

Fig. 5 | Operando characterizations on the pressure change behaviours of different Li||LTO pouch cells with various Li-based negative electrodes during cycling. a, The operando pressure sensing experiment set-up and the configuration of the Li||LTO pouch cells used for the pressure change characterizations. The split cell is constructed following literature[20]. **b**, Pressure variations and potential profiles evolution during a selected Li||LTO pouch cell discharge/charge cycle (initial stack pressure around 440 kPa, current density of 2 mA cm^{-2}, using LHCE electrolyte, potential range of 1.0–2.5 V, testing temperature at 25 °C ± 0.2 °C) using various Li metal-based negative electrodes. **c**, Schematic representation of the correlation between volume-change feature with the SEI mechanical damage and Li|electrolyte reactions for the cells containing the pristine Li and randomly distributed Li@rGO&ZnO electrodes. **d**, Pressure variations and potential profiles evolution during five consecutive Li||LTO pouch cell discharge/charge cycles (current density of 2 mA cm^{-2}, using LHCE electrolyte, potential range of 1.0–2.5 V, testing temperature at 25 °C ± 0.2 °C and initial stack pressure of around 440 kPa) using various Li metal-based negative electrodes. **e**, Schematic representation of the correlation between the 0VCCS feature with mechanical robust SEI and absence of Li|electrolyte side reactions for the cells containing the 0VCCS Li@rGO&ZnO composite at the negative electrode.

and randomly distributed Li@rGO&ZnO negative electrodes show a substantial pressure variation (Supplementary Figs. 49–54). When the Li||LTO pouch cells are cycled at current densities of 3 mA cm^{-2} and 5 mA cm^{-2}, the 0VCCS Li@rGO&ZnO negative electrode enables a zero-volume-change in the pouch cell, as shown by the constant measured pressure (Supplementary Figs. 55 and 56). Owing to the zero-volume-change feature, the SEI mechanical integrity in the 0VCCS Li@rGO&ZnO electrode is preserved (Fig. 5e).

Conclusion

In the present research work, we develop and characterize a nanoengineered Li-hosting carbon/ZnO composite electrode material with a 0VCCS design. These features enable the calculation of average CE values in the 99.9900% to 99.9999% range when the nanoengineered composite-based working electrode is tested in combination with a Li metal counter electrode and a non-aqueous electrolyte solution in low-potential coin cell configuration. Using the Li-hosting carbon/ZnO composite negative electrode in the localized highly concentrated non-aqueous electrolyte system, the negative electrode-limited Li||NCM523, Li||LFP and Li||NCM811 coin cells afford more than 80% retention of specific discharge capacity after 727 cycles (at 82.5 mA g^{-1}), 990 cycles (at 75 mA g^{-1}) and 1,020 cycles (at 188 mA g^{-1}), respectively. However, for the Li||NCM523 and Li||LFP coin cells, erratic behaviour in specific discharge capacity and CE values can be observed during

cycling, and this is likely correlated to a major extent to the unoptimized formulation of the positive electrodes. Operando battery pressure sensing characterizations, ex situ XPS, cross-sectional SEM and in situ optical microscopy measurements demonstrate the beneficial effect on the SEI and electrode mechanical integrities during cycling of the proposed nanoengineered layered cavity host structure design, as proved by comparisons between non-nanoengineered composite Li-based electrodes with similar chemical compositions but different formulations. Although the low-technology readiness level[30] proof of concept of the 0VCCS host design proposed in this research work has yielded good results, especially for low-potential lab-scale cells, further optimizations on the overall cell's architecture and material scalability must be carried out to make the proposed nanoengineered electrode material a viable candidate for use in practical Li-based non-aqueous battery cells[31].

Online content

Any methods, additional references, Nature Portfolio reporting summaries, source data, extended data, supplementary information, acknowledgements, peer review information; details of author contributions and competing interests; and statements of data and code availability are available at https://doi.org/10.1038/s41565-025-01983-4.

References

1. Kalnaus, S. et al. Solid-state batteries: the critical role of mechanics. *Science* **381**, eabg5998 (2023).
2. Zhou, G., Chen, H. & Cui, Y. Formulating energy density for designing practical lithium–sulfur batteries. *Nat. Energy* **7**, 312–319 (2022).
3. Liu, J. et al. Pathways for practical high-energy long-cycling lithium metal batteries. *Nat. Energy* **4**, 180–186 (2019).
4. Lin, D., Liu, Y. & Cui, Y. Reviving the lithium metal anode for high-energy batteries. *Nat. Nanotechnol.* **12**, 194–206 (2017).
5. Hobold, G. M. et al. Moving beyond 99.9% Coulombic efficiency for lithium anodes in liquid electrolytes. *Nat. Energy* **6**, 951–960 (2021).
6. Xiao, J. et al. Understanding and applying coulombic efficiency in lithium metal batteries. *Nat. Energy* **5**, 561–568 (2020).
7. Cheng, X., Zhang, R., Zhao, C. & Zhang, Q. Toward safe lithium metal anode in rechargeable batteries: a review. *Chem. Rev.* **117**, 10403–10473 (2017).
8. Li, Y. et al. Atomic structure of sensitive battery materials and interfaces revealed by cryo–electron microscopy. *Science* **358**, 506–510 (2017).
9. Shen, X. et al. The failure of solid electrolyte interphase on Li metal anode: structural uniformity or mechanical strength? *Adv. Energy Mater.* **10**, 1903645 (2020).
10. Peng, Y., Tamate, R. & Nishikawa, K. Review on artificial interphases for lithium metal anodes: from a mechanical perspective. *ChemElectroChem* **11**, e202400278 (2024).
11. Tikekar, M. D., Choudhury, S., Tu, Z. & Archer, L. A. Design principles for electrolytes and interfaces for stable lithium-metal batteries. *Nat. Energy* **1**, 16114 (2016).
12. Chen, H. et al. Free-standing ultrathin lithium metal–graphene oxide host foils with controllable thickness for lithium batteries. *Nat. Energy* **6**, 790–798 (2021).
13. Gao, Y. et al. Polymer–inorganic solid–electrolyte interphase for stable lithium metal batteries under lean electrolyte conditions. *Nat. Mater.* **18**, 384–389 (2019).
14. Zhang, Q. et al. Homogeneous and mechanically stable solid–electrolyte interphase enabled by trioxane-modulated electrolytes for lithium metal batteries. *Nat. Energy* **8**, 725–735 (2023).
15. Liu, Y. et al. Self-assembled monolayers direct a LiF-rich interphase toward long-life lithium metal batteries. *Science* **375**, 739–745 (2022).
16. Yu, Z. et al. Rational solvent molecule tuning for high-performance lithium metal battery electrolytes. *Nat. Energy* **7**, 94–106 (2022).
17. Zheng, Y. et al. A review of composite solid-state electrolytes for lithium batteries: fundamentals, key materials and advanced structures. *Chem. Soc. Rev.* **49**, 8790–8839 (2020).
18. Wan, J. et al. Ultrathin, flexible, solid polymer composite electrolyte enabled with aligned nanoporous host for lithium batteries. *Nat. Nanotechnol.* **14**, 705–711 (2019).
19. Fang, C. et al. Quantifying inactive lithium in lithium metal batteries. *Nature* **572**, 511–515 (2019).
20. Fang, C. et al. Pressure-tailored lithium deposition and dissolution in lithium metal batteries. *Nat. Energy* **6**, 987–994 (2021).
21. Wang, Y. et al. Emerging electrolytes with fluorinated solvents for rechargeable lithium-based batteries. *Chem. Soc. Rev.* **52**, 2713–2763 (2023).
22. Ren, X. et al. Enabling high-voltage lithium-metal batteries under practical conditions. *Joule* **3**, 1662–1676 (2019).
23. Fan, X. & Wang, C. High-voltage liquid electrolytes for Li batteries: progress and perspectives. *Chem. Soc. Rev.* **50**, 10486–10566 (2021).
24. Chen, H. et al. Electrode design with integration of high tortuosity and sulfur-philicity for high-performance lithium-sulfur battery. *Matter* **2**, 1605–1620 (2020).
25. Zhao, Y. et al. Atomic/molecular layer deposition for energy storage and conversion. *Chem. Soc. Rev.* **50**, 3889–3956 (2021).
26. Zhao, Y., Zheng, K. & Sun, X. Addressing interfacial issues in liquid-based and solid-state batteries by atomic and molecular layer deposition. *Joule* **2**, 2583–2604 (2018).
27. Adams, B. D. et al. Accurate determination of Coulombic efficiency for lithium metal anodes and lithium metal batteries. *Adv. Energy Mater.* **8**, 1702097 (2018).
28. Huang, W. et al. Onboard early detection and mitigation of lithium plating in fast-charging batteries. *Nat. Commun.* **13**, 7091 (2022).
29. Ohzuku, T., Ueda, A. & Yamamoto, N. Zero-strain insertion material of $Li[Li_{1/3}Ti_{5/3}]O_4$ for rechargeable lithium cells. *J. Electrochem Soc.* **142**, 1431–1435 (1995).
30. Frith, J. T., Lacey, M. J. & Ulissi, U. A non-academic perspective on the future of lithium-based batteries. *Nat. Commun.* **14**, 420 (2023).
31. Scurtu, R. et al. From small batteries to big claims. *Nat. Nanotechnol.* https://doi.org/10.1038/s41565-025-01906-3 (2025).
32. Zhang, Z. et al. Capturing the swelling of solid-electrolyte interphase in lithium metal batteries. *Science* **375**, 66–70 (2022).

https://doi.org/10.1038/s41565-025-01983-4

[1]State Key Laboratory of Crystal Materials, Shandong University, Jinan, People's Republic of China. [2]Institute for Advanced Interdisciplinary Research (IAIR), University of Jinan, Jinan, People's Republic of China. [3]School of Chemistry and Chemical Engineering, Shandong University, Jinan, People's Republic of China. [4]Guangdong Research Center for Interfacial Engineering of Functional Materials, College of Materials Science and Engineering, Shenzhen University, Shenzhen, People's Republic of China. [5]MOE Key Laboratory of Macromolecular Synthesis and Functionalization, Department of Polymer Science and Engineering, Key Laboratory of Adsorption and Separation Materials and Technologies of Zhejiang Province, Zhejiang University, Hangzhou, People's Republic of China. [6]Shandong Research Institute of Industrial Technology, Jinan, People's Republic of China. ✉e-mail: chaogao@zju.edu.cn; hongliu@sdu.edu.cn; haochen@sdu.edu.cn

Methods

Preparation of the 0VCCS rGO&ZnO composite material

A commercially available GO dispersion solution (Hangzhou Gaoxi Technology[33], 9 mg ml^{-1}, dispersed in water) was casted onto a glass substrate (ordered from https://shop408954563.taobao.com/, 25 cm length, 20 cm width and 1 cm thickness) using a doctor blade (Modern Instruments, GB-SZQ-1000) and dried at an atmospheric environment with a temperature of 25 °C ± 5 °C. The obtained GO film is peeled off with single-sided razor blade (Flying Eagle brand, 38 mm length, 19 mm width and 0.5 mm thickness) from the glass substrate and transferred into a nitrogen-filled glovebox (Mikrouna (Shanghai) Ind. Int. Tech., with water and O_2 content <0.01 ppm) without any special type of equipment. The porous rGO film was produced by putting the GO film in contact with a hotplate (DLAB SCIENTIFIC, MS7-H550-Pro) for 2 s, at 350 °C, placed inside the nitrogen-filled glovebox. This thermal processing of the GO film enables fast reduction and structural expansion. The expanded porous rGO film (50 µm thick, measured by SEM and micrometre screw gauge (Dongguan Sanliang Precision Measuring Instrument, MDE-25MX, measurement range is 0–25 mm, accuracy is 0.001 mm)) was subsequently placed between two stainless-steel foils (ordered from Canrd, 50 mm length, 50 mm width and 2 mm height) and polypropylene films (purchased from Canrd, MA-EN-SE-002901 16 µm) to prevent adhesion of rGO film to the stainless-steel or polypropylene substrate during the following calendaring process, and calendared down to 50 µm thickness by controlling the distance of the gap between two rollers in an air atmosphere (SHENZHEN KEJING STAR TECHNOLOGY COMPANY, GMSK-2150).

The ZnO layer was atomic layer deposited into the rGO film using an ALD machine (XIAMEN YUNMAO Technology, TEM-150) at 150 °C under nitrogen atmosphere with diethyl zinc (DEZn; Nanjing Ai Mou Yuan Scientific Equipment, 99.9999%, liquid) and deionized water (the electrical resistivity is 0.1×10^6 Ω cm at 25 °C ± 0.2 °C) as precursors. The source mass flow controller gas flow rate of nitrogen gas (JINAN DEYANG SPECIAL GAS, purity is 99.999%) was 60 standard cubic centimetre per minute (SCCM), and the source in time for DEZn and water precursor were 85 ms and 45 ms, respectively. The static transition times for DEZn and water were 3 s each, with 20 s transition purge to remove excess precursors during each pulse. DEZn alternately deposited with water for reaction, and each deposition counts as one cycle. Approximately 800 ALD cycles were needed to prepare the sample, which was allowed to cool naturally to 40 °C ± 0.1 °C at the end of the process and then collected.

Preparation of the randomly distributed rGO&ZnO composite material

Two milligrams of previously obtained 0VCCS rGO&ZnO composite material was immersed in 10 ml deionized water, and the layered structure of the composite material was deconstructed by immersing the ultrasonic vibrating rod of a 1,000 W ultrasonic machine (Ningbo Scientz Biotechnology, SCIENTZ-IID) into the rGO&ZnO composite-containing solution and sonicated for 10 min (at 25 °C ± 5 °C). Then, this solution was freeze-dried at −40 °C and vacuum pressure (≤5 Pa) using a freeze-drier (FULLKEY, FK-04 Desktop Type) to obtain randomly distributed rGO&ZnO composite material.

0VCCS Li@rGO&ZnO electrode fabrication

Ten milligrams of metallic lithium without any further treatment (Shandong Zhongshan Photoelectric Materials, 99.95%) was annealed to 350 °C after 5 min on a hotplate (DLAB SCIENTIFIC, MS7-H550-Pro) to prepare a molten lithium droplet inside an argon-filled glovebox (Mikrouna (Shanghai) Ind. Int. Tech., water and O_2 content <0.01 ppm). Using a tweezer, the 0VCCS Li@rGO&ZnO electrode was prepared by putting into contact one edge of the 50-µm-thick 0VCCS rGO&ZnO composite (2 cm^2) with the molten lithium droplet to absorb lithium into the nanoengineered rGO&ZnO composite structure. For the large-area sample (50 cm^2), 0.1 gram of metallic Li was used. The prepared rGO&ZnO composite materials were placed on another cooled stainless-steel foil (25 °C ± 5 °C) for cooling in an argon-filled glovebox (Mikrouna (Shanghai) Ind. Int. Tech., water and O_2 content <0.01 ppm) for 24 h, and stored in the glovebox for coin cell assembly.

The thickness of 0VCCS Li@rGO&ZnO electrode was measured by both SEM and micrometre screw gauge (Dongguan Sanliang Precision Measuring Instrument, MDE-25MX, measurement range is 0–25 mm, accuracy is 0.001 mm). The 50-µm-thick 0VCCS Li@rGO&ZnO electrodes were cut into circular electrodes with a diameter of 8 mm for Li||host coin cells, and circular electrodes with a diameter of 12 mm for Li||NCM523 and Li||LFP coin cells using a manual slicer (SHENZHEN KEJING STAR TECHNOLOGY COMPANY, MSK-T10). The 30-µm-thick 0VCCS Li@rGO&ZnO electrodes for Li||NCM811 coin cells were prepared by preliminarily calendaring porous rGO film to 30 µm thick, followed by same ALD, molten Li infusion and electrode cutting procedures towards circular electrodes with a diameter of 8 mm and a thickness of 30 µm. The average weight percent of Li metal in 0VCCS Li@rGO&ZnO electrode is 65.8%.

Randomly distributed Li@rGO&ZnO electrode fabrication

Ten milligrams of molten lithium was obtained by using the same lithium melting method as 0VCCS Li@rGO&ZnO electrode. In an argon-filled glovebox (Mikrouna (Shanghai) Ind. Int. Tech., water and O_2 content <0.01 ppm), the randomly distributed Li@rGO&ZnO electrode was fabricated by dispersing 5 mg of the randomly distributed rGO&ZnO composite material into the molten lithium, and then placed it on another cooled stainless-steel foil (25 °C ± 5 °C) for cooling in an argon-filled glovebox (Mikrouna (Shanghai) Ind. Int. Tech., water and O_2 content <0.01 ppm) for 24 h. The randomly distributed Li@rGO&ZnO electrode was placed between two stainless-steel plates (ordered from Canrd, 50 mm length, 50 mm width and 2 mm height) and polypropylene films (obtained from Canrd, MA-EN-SE-002901, thickness 16 µm), and then compressed to a uniform thickness of 50 µm by adjusting the gap between the rollers in an argon-filled glovebox (Mikrouna (Shanghai) Ind. Int. Tech., water and O_2 content <0.01 ppm) using a calendaring machine (model GMSK-2150, manufactured by Shenzhen Kejin Star Technology). The thickness of randomly distributed Li@rGO&ZnO electrode was measured by both SEM and micrometre screw gauge (Dongguan Sanliang Precision Measuring Instrument, MDE-25MX, measurement range is 0–25 mm, accuracy is 0.001 mm). The 50-µm-thick randomly distributed Li@rGO&ZnO electrodes were cut into circular electrodes with a diameter of 8 mm for Li||host coin cells, and circular electrodes with a diameter of 12 mm for Li||NCM523 and Li||LFP coin cells using a manual slicer (SHENZHEN KEJING STAR TECHNOLOGY COMPANY, MSK-T10). The 30-µm-thick randomly distributed Li@rGO&ZnO electrodes for Li||NCM811 coin cells were prepared by further calendaring the randomly distributed Li@rGO&ZnO electrode to 30 µm thick, followed by electrode cutting procedures towards circular electrodes with a diameter of 8 mm and a thickness of 30 µm. The average weight percent of Li metal in randomly distributed Li@rGO&ZnO electrode is 67%.

$LiFePO_4$ positive electrode fabrication

The LFP positive electrodes were fabricated by mixing with an automatic planetary centrifugal vacuum stirring defoaming machine for 1 h at an atmospheric environment with a temperature of 25 °C ± 5 °C (Shenzhen Zhidi Technology, ZD-T600C) 90 wt% carbon-coated $LiFePO_4$ powder (purchased from Canrd, MA-EN-CA-0015, D50 is 0.993 µm, purity is 98.97%), 5 wt% Super Carbon65 (purchased from Canrd, MA-EN-CO-0004, purity is 99.52%, average particle size is 150 nm) and 5 wt% polyvinylidene difluoride binder (purchased from Canrd, MA-EN-BI-0008, purity is 99.5%) in *N*-methyl pyrrolidone (Beijing InnoChem Science & Technology, purity is 99.5%, water content ≤50 ppm) to prepare a slurry. The slurry was then

cast onto carbon-coated aluminium foil (purchased from Canrd, MA-EN-CU-0003). The thickness and purity of carbon-coated layers were 1 μm and 99.5%, respectively. The thickness and purity of the uncoated Al foil were 15 μm and 99.6%, respectively, at an atmospheric environment with a temperature of 25 °C ± 5 °C, and dried in a vacuum oven (Shanghai Yiheng Scientific Instrument, DZF-6021, 133 Pa) at 60 °C for 24 h. The foils were cut into circular electrodes with a diameter of 12 mm using a manual slicer (SHENZHEN KEJING STAR TECHNOLOGY COMPANY, MSK-T10); the electrodes were stored at an argon-filled glovebox (Mikrouna (Shanghai) Ind. Int. Tech., water and O_2 content <0.01 ppm) before cell assembly. The calculated theoretical areal capacity of one single LFP electrode was around 3 mAh cm^{-2} (about 171 μm thick).

$LiNi_{0.5}Co_{0.2}Mn_{0.3}O_2$ and $LiNi_{0.8}Co_{0.1}Mn_{0.1}O_2$ positive electrode

The $LiNi_{0.5}Co_{0.2}Mn_{0.3}O_2$ (NCM523, CU-EL-PL-500202, thickness of 90 μm) and $LiNi_{0.8}Co_{0.1}Mn_{0.1}O_2$ (NCM811, SY33XX, thickness of 41 μm) positive electrode was purchased from Canrd without any drying treatment. The foils were cut into circular electrodes with a diameter of 12 mm using a manual slicer (SHENZHEN KEJING STAR TECHNOLOGY COMPANY, MSK-T10); the electrodes were stored at an argon-filled glovebox (Mikrouna (Shanghai) Ind. Int. Tech., water and O_2 content <0.01 ppm) before cell assembly.

LTO positive electrode fabrication

Double-side-coated LTO electrodes were fabricated by mixing with an automatic planetary centrifugal vacuum stirring defoaming machine for 1 h at an atmospheric environment with a temperature of 25 °C ± 5 °C (Shenzhen Zhidi Technology, ZD-T600C) 90 wt% carbon-coated LTO powder (purchased from Canrd, MA-EN-AN-0021, D50 is 1.10 μm, purity is 99%), 5 wt% Super Carbon65 (MA-EN-CO-0004, purity is 99.52%, average particle size is 150 nm) and 5 wt% polyvinylidene difluoride binder (MA-EN-BI-0008, purity is 99.5%) in *N*-methyl pyrrolidone (Beijing InnoChem Science & Technology, purity is 99.5%, water ≤50 ppm) to prepare a slurry. The slurry was casted onto one side of carbon-coated aluminium foil (purchased from Canrd, MA-EN-CU-0003). The thickness and purity of carbon-coated layers were 1 μm and 99.5%, respectively. The thickness and purity of the uncoated Al foil were 15 μm and 99.6%, respectively, at an atmospheric environment with a temperature of 25 °C ± 5 °C, and dried in a vacuum oven (Shanghai Yiheng Scientific Instrument, DZF-6021, 133 Pa) at 60 °C for 24 h. After this 24 h of vacuum drying, the LTO coating layer was fully dried as observed by a human operator. Then, the slurry was coated onto the other side of the carbon-coated aluminium foil and dried following the same procedure to obtain a double-side-coated LTO electrode. The electrode was cut into 12 mm × 12 mm sized squares, 337 μm thickness by a manual slicer (SHENZHEN KEJING STAR TECHNOLOGY COMPANY, MSK-T10); the electrodes were stored at an argon-filled glovebox (Mikrouna (Shanghai) Ind. Int. Tech., water and O_2 content <0.01 ppm) before cell assembly.

Coin cell assembly and electrochemical measurements

The Li||host coin cells with a crimping load of about 0.157 tonnes (purchased from Canrd, 304 stainless-steel material coin cell of CR2032 (including coin cell case, 15.8 mm × 1.0 mm spacer and 15.4 mm × 1.1 mm funnel spacer)) were assembled using 0VCCS rGO&ZnO (after Li being fully stripped away by the electrochemical stripping process from 0VCCS Li@rGO&ZnO through charging to 0.2 V, and confirmation of this full Li stripping by XRD spectra in Supplementary Fig. 15) in the same Li||host coin cell, randomly distributed rGO&ZnO (after Li being fully stripped away by the electrochemical stripping process from randomly distributed Li@rGO&ZnO through charging to 0.2 V, and confirmation of this full Li stripping by XRD spectra in Supplementary Fig. 15) in the same Li||host coin cell or flat copper foil (purchased from Canrd, MA-EN-CU-000202, purity is 99.99%, thickness is 9 μm, diameter is 8 mm) as working electrodes, pristine lithium metal foil (Shandong Zhongshan Photoelectric Materials, 99.95%, thickness is 500 μm, diameter is 8 mm) as the counter electrode, one layer of Celgard 2325 separator (purchased from Canrd, MA-EN-SE-000201, the porosity is 39%, average pore size is 0.028 μm, thickness is 25 μm and diameter is 19 cm) and 60 μl of non-aqueous LHCE or carbonate-based electrolyte solutions. The LHCE solution was prepared by mixing LiFSI (purchased from Canrd, MA-EN-ET-0832, the salt purity is 99.5%, water content ≤100 ppm, used without any treatment), DME (purchased from Beijing InnoChem Science & Technology without any treatment, purity is 99.5%, water content ≤50 ppm) and TTE (purchased from Canrd, purity is 97%, water content not provided by the supplier), continuously drying with 500 μm pure Li foil for 7 days and then using it until the Li no longer changes colour, with a molar ratio of 1:1.2:3 in an argon-filled glovebox (Mikrouna (Shanghai) Ind. Int. Tech., water and O_2 content <0.01 ppm). The entire process uses a mechanical pipette and the corresponding pipette tip (all of them purchased from DLAB SCIENTIFIC) to draw the solvent. The electrolyte was prepared in an experiment-grade glass bottle (purchased from Canrd, 25 ml) made of high-quality borosilicate glass. It is stirred by a magnetic bar made of polytetrafluoroethylene (purchased from Canrd, C type, 10 mm length, 4 mm width and 4 mm height) and a magnetic stirrer (XIUILAB, MS-2B) is used. The carbonate-based electrolyte (1 molar concentration) solution was prepared by mixing 89 wt% of 1 M $LiPF_6$ in EC/DEC solution (this solution is purchased from Canrd, MA-EN-ET-0202, water content ≤20 ppm, used without any treatment) with a 10 wt% of FEC (purchased from Canrd, MA-EN-ET-0893, purity is 99.95%, water content ≤50 ppm, used without any treatment) and 1 wt% of VC (purchased from Canrd, MA-EN-ET-0892, purity is 99.9%, water content ≤30 ppm, used without any treatment) additives in an argon-filled glovebox (Mikrouna (Shanghai) Ind. Int. Tech., water and O_2 content <0.01 ppm). The pipette, new pipette tips and stirrer used are the same as those in LHCE preparation procedures. The difference was that plastic bottles for carbonate electrolyte storage were made of high-density polyethylene (purchased from Canrd, MA-CM-PL-001101). The Li plating/stripping CE is calculated by dividing the discharging capacity by the charging capacity in the Li||host coin cells. Because the lithium amount at the counter Li electrode was excessive, therefore the calculated CE is for the Li plating/stripping CE in the host[6]. The Li||host cells were cycled at 1 mA cm^2 or 3 mA cm^2 for long cycling with a temperature of 25 °C ± 0.2 °C in a constant-temperature-controlling environmental chamber (http://www.wuhanyueda.com/, YDC-300HT). For the cycling process, the areal capacity for Li plating was controlled at a constant current density and the cell's cut-off potential was 90 mV or 1 V for the cells with the LHCE, and 160 mV for the cells with the carbonate electrolyte. The Aurbach CE[27] test was conducted by first depositing lithium onto the host or Cu substrate using a total charge (Q_T) to establish a lithium reservoir. A subset of this charge (Q_C) was then cycled between the working and counter electrodes for 10 cycles. After cycling, the remaining lithium was completely stripped to the upper cut-off voltage, with the final stripping charge (Q_S) quantifying the residual lithium. The charge cut-off voltages of 0.09 V and 1.0 V were both tested in different experiments in Supplementary Figs. 23 and 24. The average CE over 10 cycles was calculated:

$$CE_{average} = \frac{10Q_C + Q_S}{10Q_C + Q_T}$$

Li||NCM523 coin cells (coin cell case purchased from Canrd), with a 15.8 mm (diameter) × 1.0 mm (thickness) regular spacer and a 15.4 mm (diameter) × 1.1 mm (thickness) funnel spacer, are made of 316 stainless steel. The coin cell fabrication is realized by putting the following materials into negative case by sequence: one funnel piece, one regular spacer, negative electrode (Li metal-containing negative electrode, 50-μm-thick 0VCCS Li@rGO&ZnO with areal capacity of

7.036 mAh cm^{-2}, 50-µm-thick randomly distributed Li@rGO&ZnO host with areal capacity of 7 mAh cm^{-2} or 50-µm-thick pristine Li metal anode with areal capacity of 10 mAh cm^{-2}), one layer of Celgard 2325 separator, 60 µl LHCE solution injected by pipette and positive NCM523 electrode (purchased from Canrd, CU-EL-PL-500202). Then the coin cell was covered by the positive case, sealed by the compact hydraulic coin cell sealing press machine with a crimping load of about 0.157 tonnes (purchased from SHENZHEN KEJING STAR TECHNOLOGY COMPANY, MSK-110) inside an argon-filled glovebox (Mikrouna (Shanghai) Ind. Int. Tech., with water and O_2 content <0.01 ppm). The assembled Li||NCM523 coin cells were charged to the upper cut-off potential of 4.35 V at a specific current of 8.25 mA g^{-1} and then discharged to the lower cut-off potential of 3.0 V at a specific current of 8.25 mA g^{-1} in the first 2 cycles. After the above 'activation' process, the Li||NCM523 coin cells were cycled at a constant specific current of 82.5 mA g^{-1} between 3.0 V and 4.35 V for long cycling. The capacity retention was achieved by dividing the discharge capacity of the initial cycle under the condition of specific current of 82.5 mA g^{-1} (156.483 mAh g^{-1}, 1st cycle in Fig. 3e and 3rd cycle of the total battery cycling condition, as there existed 2 activation cycles at a specific current of 8.25 mA g^{-1} shown in Supplementary Fig. 29) by that of the final cycle (727th cycle in Fig. 3e, 138.924 mAh g^{-1}) under a specific current of 82.5 mA g^{-1}.

Li||NCM811 coin cells (assembled using the same method as the Li||NCM523 coin cells) were assembled using NCM811-based positive electrodes (1.5 mAh cm^{-2}, purchased from Canrd, SY33XX), one layer of Celgard 2325 separator, 60 µl LHCE solution and Li metal-containing negative electrode (30-µm-thick 0VCCS Li@rGO&ZnO with areal capacity of 3.71 mAh cm^{-2}, 30-µm-thick randomly distributed Li@rGO&ZnO host with areal capacity of 3.74 mAh cm^{-2} or 20-µm-thick pristine Li metal anode with areal capacity of 4 mAh cm^{-2}). The assembled Li||NCM811 coin cells were charged to the upper cut-off potential of 4.3 V at a specific current of 9.4 mA g^{-1} and then discharged to the lower cut-off potential of 3.0 V at a specific current of 9.4 mA g^{-1} in the initial 2 activation cycles. After the above 'activation' process, the Li||NCM811 coin cells were cycled at a constant specific current of 188 mA g^{-1} between 3.0 V and 4.3 V for long cycling. The capacity retention was achieved by dividing the discharge capacity of the initial cycle (187.189 mAh g^{-1}, 1st cycle in Fig. 3g and 3rd cycle of the total battery cycling condition, as there exist 2 activation cycles at a specific current of 9.4 mA g^{-1} shown in Supplementary Fig. 43) by that of the final cycle (1,020th cycle here, 154.248 mAh g^{-1}) under a specific current of 188 mA g^{-1}.

Li||LFP coin cells (assembled using the same method reported above for the Li||NCM523 coin cells) were assembled using LFP-based positive electrodes (3 mAh cm^{-2}, fabricated as reported above), one layer of Celgard 2325 separator, 60 µl LHCE solution and Li metal-containing negative electrode (50-µm-thick 0VCCS Li@rGO&ZnO with areal capacity of 7.036 mAh cm^{-2}, 50-µm-thick randomly distributed Li@rGO&ZnO host with areal capacity of 7.000 mAh cm^{-2} or 50-µm-thick pristine Li metal anode with areal capacity of 10 mAh cm^{-2}). The assembled Li||LFP coin cells were charged to the upper cut-off potential of 4.0 V at a specific current of 7.5 mA g^{-1} and then discharged to the lower cut-off potential of 2.5 V at a specific current of 7.5 mA g^{-1} in the initial 2 activation cycles. After the above 'activation' process, the Li||LFP coin cells were cycled at a constant specific current of 75 mA g^{-1} between 2.5 V and 4.0 V for long cycling. The capacity retention was achieved by dividing the discharge capacity of the initial cycle (140.684 mAh g^{-1}, 1st cycle in Fig. 3f and 3rd cycle of the total battery cycling condition, as there existed 2 activation cycles at a specific current of 7.5 mA g^{-1} shown in Supplementary Fig. 36) by that of the final cycle (990th cycle, 123.694 mAh g^{-1}).

All the electrochemical measurements were carried out using LAND battery testing systems (Wuhan Land Electronics, CT3002A, 5 V, 1 mA and 10 mA 8C1U) at a constant temperature chamber with a temperature (http://www.wuhanyueda.com/, YDC-300HT) of 25 °C ± 0.2 °C. No less than five paralleling cells were tested for a single electrochemical experiment, and the data presented in the paper's plots represent a median result of all the cells tested for a single electrochemical experiment.

Pouch cell fabrication and electrochemical measurements

Li||LTO lab-scale pouch cells were assembled in an argon-filled glovebox (Mikrouna (Shanghai) Ind. Int. Tech., water and O_2 content <0.01 ppm) using LTO-based double-side-coated positive electrodes (cutted into 12 mm × 12 mm sized squares) with a manual slicer (SHENZHEN KEJING STAR TECHNOLOGY COMPANY, MSK-T10, sandwiched with a Celgard 2325 separator (diameter of 19 mm and a thickness of 25 µm) and 12 mm × 12 mm sized squared Li metal-based negative electrodes (50-µm-thick 0VCCS Li@rGO&ZnO, 50-µm-thick randomly distributed Li@rGO&ZnO or 50-µm-thick pure Li metal electrodes) with a manual slicer (SHENZHEN KEJING STAR TECHNOLOGY COMPANY, MSK-T10) before being stacked and assembled into the battery core. The stacking sequence is one copper foil current collector, one negative electrode, one layer of separator, one double-side positive electrode, one layer of separator and one negative electrode. In total, four copper foil current collectors, three double-side positive electrodes, six single-layer negative electrodes and six separator layers were assembled into the pouch cell. The cell core was then sealed in an aluminium plastic packing film (purchased from Canrd, MA-EN-FC-001103), and 500 µl LHCE solution (see above for the exact composition) was injected before final sealing using a vacuum pre-sealing machine (SHENZHEN KEJING STAR TECHNOLOGY COMPANY, MSK-115A-III). These pouch cells were rested at open circuit potential for 24 h under a temperature of 25 °C ± 0.2 °C before 2 mA cm^{-2} charge/discharge cycling between 1.0 V and 2.5 V inside a constant-temperature-controlling chamber (http://www.wuhanyueda.com/, YDC-300HT) with a temperature of 25 °C ± 0.2 °C.

Operando pressure measurement

The operando battery pressure sensing equipment was purchased from SCI Materials Hub (www.scimaterials.cn). A metal block with a size slightly larger than the cell core was attached to the cell as a force-distribution plate. A button-style pressure sensor was attached to the metal block. The entire stack was then clamped with an initial stack pressure of about 440 kPa or 90 kPa (Fig. 5a). Each pouch cell contains an empty pocket to prevent any pressure effect generated by the gas produced within the cell. If any gas is generated during battery operation, it will be pushed into the pocket owing to the compressive force applied to the cell. Thus, the pressure measurement was not interfered with by any gas generation. However, we did not observe any notable gas generation during battery testing (visual inspection on the appearance of battery pack bloating by the naked eye of the human operator). A real-time data collector (monitor the stack pressure values in real time and record it during the battery cycling process) was used to record cells' potential and pressure variations throughout the electrochemical measurements[20].

Electrolyte absorption test

A 1.5 ml centrifuge tube (Biosharp, BS-15-M) was cutted at its bottom using a Flying Eagle single-sided razor blade (38 mm length, 19 mm width and 0.5 mm thickness). This cutted centrifuge tube was tightly placed in inverted position on the 0VCCS rGO&ZnO or randomly distributed rGO&ZnO host, and a lab tissue paper (the main component is plant cellulose fibre, for collecting the electrolyte infiltrated through the host) and black wood substrate of the fume hood (Wuxi Puruida Laboratory Equipment, for contrast visualization via semi-transparency of the lab tissue paper upon electrolyte wetting) was put underneath the host in an atmospheric environment with a temperature of 25 °C ± 5 °C, as the electrolyte-swelled lab tissue paper can realize minor semi-transparence for showing the colour of black substrate underneath. LHCE solution (1 ml) was injected into

the centrifuge tube through the cutted hole by a syringe (BERPU, 2 ml 2-part syringe). This observation was conducted through a human operator, and imaging was carried out using the camera for initial state (0 s), and 5 s, 20 s, 30 s and 60 s after placing the electrolyte. No electrolyte permeation was detected for the 0VCCS rGO&ZnO host, while the randomly distributed rGO&ZnO host shows a continuous and detectable amount of permeated electrolyte.

Titration-collection-gas chromatography technique (TCGC) characterization

The TCGC characterization was conducted following literature procedures[19]. After discharging 1 mAh cm^{-2} or 3 mAh cm^{-2} capacity or charging to 0.09 V or 1.0 V (applying a current density of 1 mA cm^{-2}), Li||0VCCS rGO@ZnO coin cells are disassembled in an Ar-filled glovebox. In the Ar-filled glovebox (Mikrouna (Shanghai) Ind. Int. Tech., water and O_2 content <0.01 ppm), the 0VCCS rGO@ZnO electrodes were collected and directly transferred into a 25 ml titration reaction glass Schlenk bottle (purchased from TCHONGQING XINWEIER GLASS) (used as Li^0 conversion reaction bottle) and sealed (rubber stoppers of uniform bottle mouth size). Then the Li^0 conversion reaction bottle was connected to the gas diffusion device (purchased from China Education Au-light, CEL-PAEM-D8mini) and pre-vacuumed. After completing these steps, 5 ml of deionized water was injected into the reaction bottle to convert the residual metallic Li^0 into hydrogen gas. The hydrogen gas generated by the reaction was collected by a glass pipeline and then continuously injected into the gas chromatography (purchased from Japan SHIMADZU, GC-2014) by an automatic sampler (purchased from China Education Au-light, CEL-GSOA-20V). The content of the metallic Li^0 was determined by converting the corresponding H_2 amount according to a pre-established standard calibration curve. Detailed calculation steps are shown in Supplementary Note 2.

In situ optical microscopy characterization

In situ optical microscopy characterization was performed using an upright microscope (Anhui Yueshi Precision Instrument, TM520R) equipped with a 20× long working distance objective (Anhui Yueshi Precision Instrument, numerical aperture ≥ 0.45, working distance ≥ 13 mm). Lithium plating/stripping experiments were conducted within a custom hermetically sealed optical cell as an in situ dendrite observation system (Anhui Yueshi Precision Instrument, ISC03, 50 mm length, 50 mm width and 18 mm thickness). The cell incorporated two 1.0-mm-thick fused quartz windows, a lithium foil counter/reference electrode (Shandong Zhongshan Photoelectric Materials, 99.95%), 0VCCS Li@rGO&ZnO host or pristine Li working electrode saturated with 1 ml LHCE electrolyte. The optical cell was assembled and electrolyte-injected inside an Ar-filled glovebox (Mikrouna (Shanghai) Ind. Int. Tech., water and O_2 content <0.01 ppm). The sealed cell was then transferred to the microscope stage at an atmospheric environment with a temperature of 25 °C ± 1 °C. After assembly, the external galvanostatic plating (1 mA cm^{-2} or 3 mA cm^{-2} constant current, areal capacity of 1 mAh cm^{-2}) was made via spring-loaded titanium pistons electrical connections with LAND battery testing systems (CT3002A, 5 V, 1 mA and 10 mA 8C1U). Real-time monitoring commenced simultaneously with current application. Time-lapse image sequences were acquired at different times during the plating procedure.

Physicochemical characterizations

The morphology of the pristine and cycled electrode materials was characterized by SEM (Hitachi S-4800). The composition of the samples was examined by XRD (Rigaku SmartLab), Cu Kα radiation (λ = 1.5418 Å). The XPS measurements of the cycled electrodes to investigate the SEI composition were carried out using ESCALAB 250 with Al Kα radiation. The sputtering process (under the conditions of argon purging, 4 K eV and 60 s each time) was used to remove the characterized surface from the electrode material to carry out XPS measurements on the inner layers. The binding energies were calibrated with respect to the C 1*s* peak at 284.6 eV. High-resolution field emission TEM micrographs were collected with ThermoFisher F200XG2. AFM micrographs were collected with BioScope Resolve. A relative calibration approach was used: the deflection sensitivity of the tip was first calibrated using a sapphire reference sample, followed by characterization of tip indentation depth and radius of curvature with a standard sample, before testing the target specimens. AFM force–distance curves were analysed using the Derjaguin–Muller–Toporov model to determine Young's modulus[34]. All the cycled electrodes were rinsed with pure anhydrous DME solvent (purchased from Beijing InnoChem Science & Technology without any treatment, purity is 99.5%, water content ≤50 ppm; 100 µl DME injected onto the electrode surface at a uniform rate within 5 s; each electrode is rinsed three times, with a 1 min interval each time) to remove residual LiFSI[8], transferred into the vacuum transfer chamber of the glovebox and pumped for 30 min (Mikrouna (Shanghai) Ind. Int. Tech., with water and O_2 content <0.01 ppm). During the SEM and AFM testing process, the electrode was pasted to the sample holder (SEM and AFM) and then was putted into a petri dish inside an aluminium plastic packing film (purchased from Canrd, MA-EN-FC-001103), and four sides of this bag were sealed by a single-station heat sealing machine (SHENZHEN KEJING STAR TECHNOLOGY COMPANY, MSK-140) in an argon-filled glovebox (Mikrouna (Shanghai) Ind. Int. Tech., water and O_2 content <0.01 ppm). Before the SEM and AFM test, the electrode was taken out from the cutted aluminium plastic packing bag for transferring to the test chamber of the equipment at the fastest speed with minor exposure to air for 5–10 s. The testing process was carried out under vacuum (for SEM) or argon gas (for AFM) conditions. Before the TEM test, 10 mg portions of rGO and rGO@ZnO composite were separately dispersed in 10 ml anhydrous ethanol (purchased from Sinopharm Chemical Reagent, purity ≥99.7%) within glass bottle (purchased from Canrd, 25 ml). After 5 min ultrasonication (Ningbo Scientz Biotechnology, SCIENTZ-IID), 10 µl aliquots of each suspension were deposited onto Lacey Formvar/carbon film-coated grids (purchased from Zhongjing Keyi Technology, BZ110135a, 300 mesh). The grids were air-dried (25 °C ± 5 °C, air humidity is 45–55%) for 30 min in a petri dish before being loaded into the TEM sample holder. Given the oxidative stability and moisture resistance of both rGO and rGO@ZnO composites, samples were handled under ambient conditions without encapsulation. During the XRD test, the electrode was tightly pre-sealed with polyimide tape (purchased from Canrd, MA-EN-FC-0004, 20 mm length, 20 mm width and 26 µm thick) inside the argon-filled glovebox, to confirm the absence of exposure to the air during transferring and characterization. All of the sealing processes were carried out in an argon-filled glovebox (Mikrouna (Shanghai) Ind. Int. Tech., water and O_2 content <0.01 ppm). For the XPS characterization, based on the characteristics of the ESCALAB 250 XPS machine, we use an XPS transfer chamber (Beijing Billison Technology) that paste the electrode onto the chamber stage using carbon tape inside the argon-filled glovebox (Mikrouna (Shanghai) Ind. Int. Tech., water and O_2 content <0.01 ppm), vacuumed evacuate at −0.1 MPa versus ambient pressure for 5 min to seal the transfer chamber in the vacuum transfer chamber of the glovebox, and transferred into the XPS machine without exposing to air.

COMSOL simulation

Transient simulations of the electrochemical secondary current distribution and diffusion were carried out in a two-dimensional model using finite element simulation to simulate the changes in layer morphology during electrochemical deposition of different electrode structures (undulating layer stacked structures (denoted as 0VCCS rGO&ZnO), randomly distributed sheet stacked structures (denoted as random rGO&ZnO)) and the diffusion infiltration process of the

electrolyte in different electrode structures. Specifically, the electric field in the electrolyte region follows the intrinsic relation, the electrochemical process on the electrode surface ($Li^+ + e^- = Li$) follows the boundary conditions of the Butler–Volmer kinetic equation, and the electrode potential follows the Nernst equation; the migration of ions follows Fick's law and the Nernst–Einstein relation, and the left and right boundaries are set as the periodic boundary conditions, and the upper boundary is the open boundary. The solution process is based on free triangular meshing and boundary layers are set up on the electrode surface to make the boundary physical field converge accurately. The solver uses PARDISO (parallel sparse direct solver) and converges based on Newton's method, and the relative tolerance is set to 1E-6 to ensure the accuracy of the results.

Data availability

The data that support the plots within this paper and other findings of this study are available from the corresponding authors upon reasonable request. Source data are provided with this paper.

References

33. Hangzhou Gaoxi Technology Co., Ltd. https://www.gaoxitech.com/en/special1.html (2025).
34. Caicedo, J. D., Pandoli, O. G., Hernandez, J. D. & Frota, M. N. Nanotechnology measurements of the Young's modulus of polymeric materials. *J. Phys. Conf. Ser.* **1826**, 012004 (2021).

Acknowledgements

This work is supported by the National Natural Science Foundation of China (grant number 52402281, received by H.C.), the Shandong Provincial Natural Science Foundation (grant number ZR2023ZD52, received by H.C.), the Shandong Provincial Natural Science Foundation for Excellent Young Scientists Fund Program (Overseas) (grant number 2022HWYQ-051, received by H.C.), the Taishan Scholars Program (received by H.C.), the Qilu Young Scholar Funding and Outstanding Young Scholar Funding of Shandong University (received by H.C.), and the Fundamental Research Funds for the Central Universities (226-2024-00074 and 226-2024-00172, received by C.G.). We acknowledge the facilities of the Electron Microscopy Center of Shandong University.

Author contributions

L.D., C.G. and H.C. conceived the idea for the project. L.D., Z.W. and H.Q. fabricated the electrodes. L.D., Y.L., D.Q. and K.-P.S. conducted the SEM, TEM, AFM and XPS characterizations. L.-T.D. and J.-J.W. conducted the XRD characterizations. L.D., J.Z., Y.S. and S.W. conducted the electrochemical measurements. L.D., Y.L. and Y.Y. conducted the titration-collection-gas chromatography technique (AAC-TCGC) characterization. Y.X., J.Y. and Z.Z. conducted the ALD. L.D., H.L., C.G. and H.C. wrote the paper. All authors discussed the results and commented on the paper at all stages.

Competing interests

The authors declare no competing interests.

Additional information

Supplementary information The online version contains supplementary material available at https://doi.org/10.1038/s41565-025-01983-4.

Correspondence and requests for materials should be addressed to Chao Gao, Hong Liu or Hao Chen.

Peer review information *Nature Nanotechnology* thanks the anonymous reviewer(s) for their contribution to the peer review of this work.